Contents lists available at ScienceDirect

Applied Catalysis B: Environment and Energy

Dual-active-center in Co doping LiNbO$_3$ for enhanced CO$_2$ photoreduction in pure water

Liangling Sun [a], Hairui Cai [a], Bin Wang [a], Jingwen Xu [a], Xiaoxiao Zeng [a], Chao Liang [a,*], Zhimao Yang [a,*], Shengchun Yang [a,b,**]

[a] MOE Key Laboratory for Non-equilibrium Synthesis and Modulation of Condensed Matter, State Key Laboratory for Mechanical Behavior of Materials, School of Physics, Xi'an Jiaotong University, Xi'an 710049, People's Republic of China
[b] National Innovation Platform (Center) for Industry-Education Integration of Energy Storage Technology, Xi'an Jiaotong University, Xi'an 710049, People's Republic of China

ARTICLE INFO

ABSTRACT

Photocatalysis techniques for converting CO$_2$ into valuable chemicals driven by solar irradiation has drawn increasing attention. While many photocatalysts often generate by-products that pose challenges for the subsequent synthesis of more complex products. Therefore, designing catalysts with both high selectivity and activity has become a critical issue. Our study reveals that the formation of dual-active-center in Co doping LiNbO$_3$ (Co-LN) photocatalyst greatly improves the yield and selectivity of CO in photoreduction of CO$_2$ in pure water at room temperature without requiring additional sacrificial agents. The extended X-ray absorption fine structure spectroscopy together with some *in-situ* measurement techniques and theoretical calculations reveal that the dual-active-center of oxygen vacancy and Co-dopant stabilizes the *CO$_2$ and *CO intermediates, respectively, which regulates the rate-limiting step and facilitates the high activity and selectivity. This research will stimulate in-depth research on the use of efficient niobate materials for the photocatalytic conversion of CO$_2$.

1. Introduction

Photocatalytic reduction of carbon dioxide (CO$_2$) into valuable carbon-based fuels and raw materials by using renewable solar energy is a highly promising carbon-negative technology for clean energy conversion and environmental protection [1–5]. However, the performance of photocatalysts in CO$_2$ photoreduction still faces challenges such as product selectivity, low efficiency, and unsustainable reactions [6–8]. As a result, considerable efforts have been devoted to discovering new catalysts or optimizing existing ones [9–12].

Perovskite oxides are known for their highly adjustable electronic structure achieved by doping different cations or modifying the A- or/ and B-site cations [13–15]. This adjustability raises expectations that perovskite oxides can exhibit excellent photocatalytic performance through regulation of their electronic structures. For instance, Teramura et al. demonstrated that the band gap of tantalate perovskite could be significantly influenced by the A-site species, with LiTaO$_3$ having the largest band gap (4.9 eV) followed by NaTaO$_3$ (4.1 eV), and KTaO$_3$ (3.7

eV) [16]. This band gap variation also correlated with the photocatalytic activity in CO$_2$ conversion. Raziq et al. found that doping Sr$_2$CoTaO$_6$ with C and S atoms resulted in hybridized states above and below the Fermi level, respectively, leading to reduced band gap and enhanced charge-carrier mobility for CO$_2$ photoreduction (CO yield: 5 µmol·g^{-1}·h^{-1}; CH$_4$ yield: 38.89 µmol·g^{-1}·h^{-1}) [13]. Nevertheless, the selectivity and efficiency of photocatalytic reactions still need to be further improved to meet the requirement of practical applications.

The oxygen vacancies (V$_O$) in perovskite usually lead to a smaller band gap and stronger reduction capability, and significantly reducing the dissociation energies of H$_2$O, thus accelerating the kinetics of H$_2$O oxidation reactions, thereby providing more protons for subsequent reaction steps [17,18]. Numerous studies have focused on tuning V$_O$ to improve the photocatalytic properties of perovskite catalysts [19,20]. For example, Yu et al. prepared Vo-abundant Sr$_2$Bi$_2$Nb$_2$TiO$_{12}$ by *in-situ* treatment of Sr$_2$Bi$_2$Nb$_2$TiO$_{12}$ nanosheets with glyoxal, which extended photo adsorption and formed stronger covalent interactions between Vo and absorbed CO$_2$ molecules [21]. Yang et al. reported that increasing

---

V_O content in $BaTiO_3$ through a polyol system enhanced the adsorption capacity of CO_2 and improved the ability to separate and transfer photoinduced electron-hole pairs [22]. Similar phenomena have been observed in other catalysts, such as V_O-rich NiO/Co_3O_4 [23,24] and Cu-introduced CeO_{2-x} [25]. Although pioneering research on V_O has improved the photocatalytic performance of materials to some extent, there is still a lack of understanding regarding the mechanisms underlying further optimization of V_O-containing materials, including the regulation of product selectivity and yield through doping.

Lithium niobate ($LiNbO_3$, LN) has attracted much attention due to its various photoelectric properties, such as piezoelectric, electro-optic, photorefractive, photovoltaic, photoelastic effects and so on [26,27]. The optical energy bandgap of LN is 4.0 eV, indicating its photo-absorption in the UV region. Although this typically limits its visible-light photocatalytic activity, various techniques such as doping or nano-sizing induced defect chemistry have been adopted to extend its photo response [28,29]. As a result, metal-doped LN with an expanded photo response band has been extensively studied for applications such as organic pollutant degradation and water splitting [30–32]. In this work, we significantly extended the photo absorption capability of LN by doping it with Co atom and reducing the perovskite size, resulting in a reduced optical energy bandgap of 3.49 eV. Additionally, the concentration of V_O in LN crystal was significantly increased. As a result, the Co-doped LN exhibited remarkable photocatalytic activity and nearly 100 % selectivity for CO in the photoreduction of CO_2 using pure water (gas-solid, water vapor), without the need for co-catalysts or sacrificial agents. The CO_2 photoreduction rate of Co-LN was approximately 3.8 times higher than that of pristine LN (71.1 μmol g^{-1} h^{-1} for Co-LN vis. 18.9 μmol g^{-1} h^{-1} for LN). The extended X-ray absorption fine structure spectroscopy (EXAFS) and in-situ measurement techniques, including XPS, ESR, and FTIR, along with the theoretical calculations, provided valuable insights into the underlying mechanisms behind the improved performance. These analyses revealed that the synergistic effect of the V_O-Co dual-center stabilized the $*CO_2$ and $*CO$ intermediates, respectively, and thus reduced the Gibbs free energy (ΔG) of the rate-limiting step, thereby facilitating a 100 % selectivity in the photoreduction of CO_2 to CO. This work may provide new opportunities to expand the family of photocatalysts used for CO_2 reduction and stimulate an in-depth research on the use of new and efficient niobate for photocatalytic conversion of CO_2.

2. Experimental section

2.1. Synthesis of LN and Co-LN

LN and Co-LN nanoparticles were prepared through non-aqueous sol-gel route. In brief, a certain amount of $Nb(OC_2H_5)_5$ and Li(acac) were dissolved in 20 mL of benzyl alcohol and stirred for 6 h at room temperature to obtain 40 mM $Nb(OC_2H_5)_5$ and 70 mM Li(acac) solution. The resulting mixture was transferred to a 50 mL Para-polystyrene (PPL) autoclave and heated at 220 °C for 4 days with a temperature ramping rate of 5 °C min^{-1}. After natural cooling to room temperature, precipitates were isolated from the reaction mixture by centrifugation at 9000 r/min for 5 min. The obtained solids were washed five more times with absolute ethanol and deionized water. Finally, the purified product was dried at 60 °C for 2 h to remove moisture present from the purification process. Co-doped catalysts are prepared using the same method except for the addition of different amounts of $Co(acac)_3$. The addition amounts of Co were 0.1 mol%, 0.5 mol%, and 1 mol% of Nb, denoted as 0.1 %Co-LN, 0.5 %Co-LN, and 1 %Co-LN, respectively.

2.2. Photoelectrochemical measurements

Transient photocurrent response and electrochemical impedance tests were carried out in a standard three-electrode system with an electrochemical workstation (CHI660E, China). 0.5 M Na_2SO_4 aqueous solution was used as electrolyte with Pt net and Ag/AgCl standard electrode as counter and reference electrode, respectively. A 300 W Xenon lamp (PLS-SXE300, Perfectlight, China) was used as light source and positioned 10 cm in front of the electrolytic cell. Transient photocurrent response was obtained under a 0.5 eV starting voltage with light source turning on and off at interval of 50 s. Electrochemical impedance was captured under 5 mV voltage amplitude with frequency range of 10^{-2}-10^5 Hz. The work electrode was prepared as follows: the corresponding photocatalyst (2 mg) were fully dispersed in water/isopropanol mixed solvent (4:1; v/v) isopropyl alcohol by ultrasound for 5 min. After that, 10 uL Nafion were dispersed in the mixture solution for another 5 min ultrasound. Subsequently, 50 uL of the mixture was evenly coated onto a 1 cm × 1.5 cm ITO glass electrode (active area, 1 cm^2). The resulting work electrode was naturally dried in air for 1 h.

2.3. Photocatalytic CO_2 reduction

The photocatalytic CO_2 reduction test was executed in glass photoreactor (120 mL) with a quartz window on the top of reactor. The lower and higher openings are used to feed in and out the condensed water to keep the temperature in the reactor constant. The photograph photocatalytic CO_2 reduction unit is shown in Fig. S2. The catalyst (1.3 mg) was evenly sprayed on a piece of glass (2.5 × 2.5 cm) by a high-pressure airbrush (MOSHEN Vinci MS 1001 0.2). Then, the glass is placed at the bottom of the reactor. The reactor was evacuated buy a vacuum pump, and the high purity CO_2 gas (99.999 %) was purged into the system to clean the reactor. The reactor was cleaned by CO_2 for at least four times. And then 10 uL deionized water was injected into a reaction reactor. After that the reactor was left to rest overnight to obtain the adsorption balance of CO_2 and water vapor. The reaction process adopted the PLS-SXE 300UV model xenon lamp light source (Beijing Perfectlight Technology Co. Ltd). In addition to the light intensity test, unless otherwise specified, the relevant tests adopt 287 mW cm^{-2} light intensity. The gas in the reactor was extracted for 400 uL through a handheld gas sampler for gas chromatographic analysis. The gas product was detected by a North Point NP-GC-901A gas chromatograph (N_2 as carrier gas, hydrogen flame ionization detectors (FID) per 1 h. FID is equipped with chromatographic columns for TDX-01. The method of photothermal/thermal catalytic CO_2 reduction is similar to that of photocatalytic reduction. The only difference is that the reactor is insulated in a bath of oil at a certain temperature (100, 150, 200, 250, and 275 °C) for one hour before switched on the light.

The selectivity of the productions was deduced according to the following equation [33]:

$$\% \text{ of } CH_4 \text{ selectivity } = \frac{8N_{CH_4}}{8N_{CH_4} + 2N_{CO}} \tag{1}$$

$$\% \text{ of } CO \text{ selectivity } = \frac{2N_{CO}}{8N_{CH_4} + 2N_{CO}} \tag{2}$$

in which N_{CH_4} and N_{CO} stand for the yield of reactively CH_4 and CO respectively.

3. Results and discussion

The synthesis of LN and x%Co-LN was carried out through a non-aqueous sol-gel route (Fig. 1a) with a stoichiometric ratio of precursors, except for cobalt. X-ray diffraction (XRD) patterns (Fig. 1b) and corresponding Rietveld refinement (Fig. 1c and S3, and Table S1) demonstrate that the crystal structures of LN, 0.1 %Co-LN, 0.5 %Co-LN, and 1 %Co-LN match well with the standard card (JCPDS:20-0631) for $LiNbO_3$ perovskite structure. As can be seen in Table S2, inductively coupled plasma-mass spectrometry (ICP-MS) measurement reveals the Co content of 0.1 %Co-LN, 0.5 %Co-LN, and 1 %Co-LN are 0.088 wt%, 0.60 wt%,1.18 wt%, respectively. The volumes of the xCo-LN (refinement results) decrease with the increase of Co doping amount,
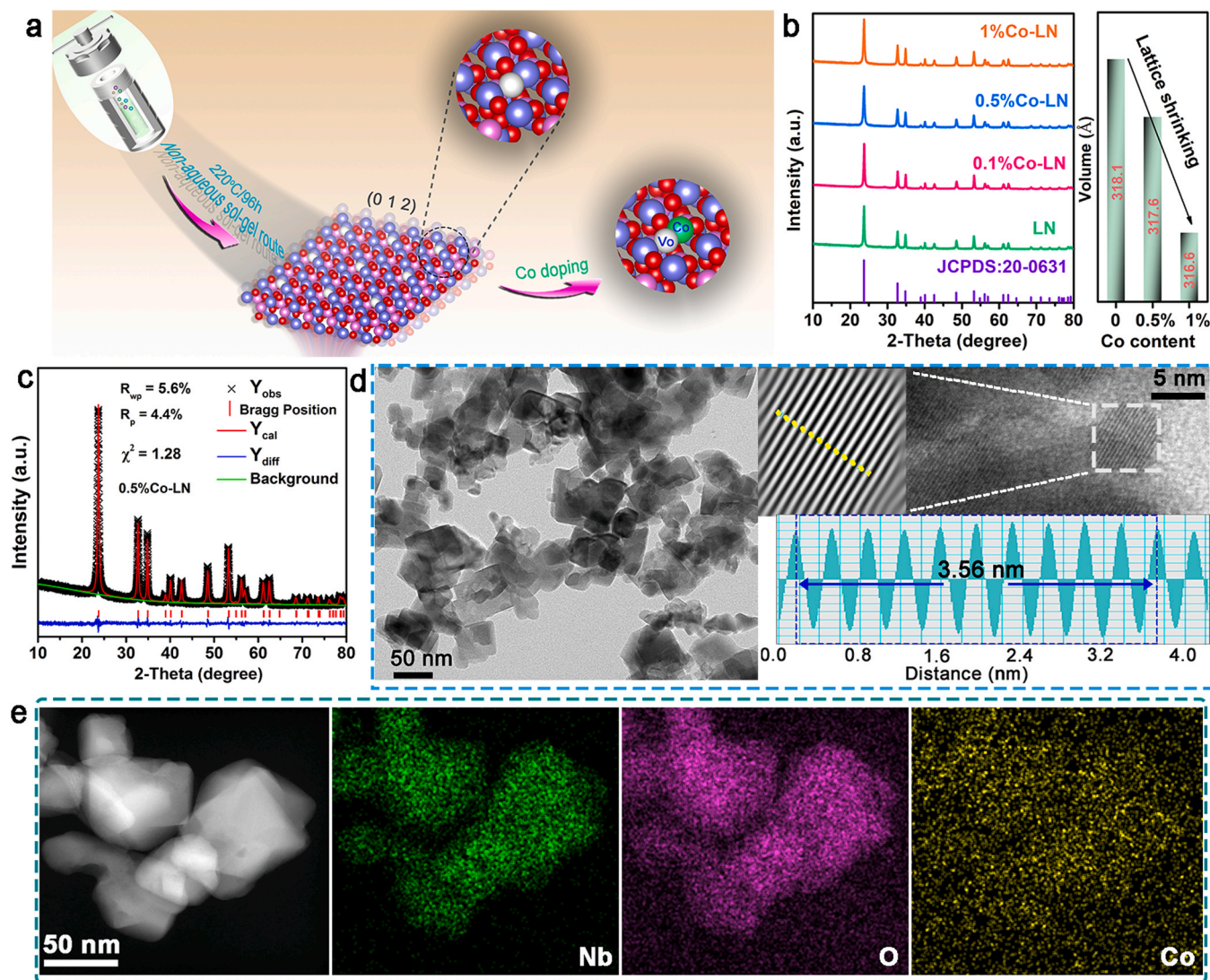
Fig. 1. a) Scheme for LN and Co-LN crystal structure; Li, Nb, O, Co and oxygen vacancy are denoted as pink, purple, red, green and white balls, respectively. b) XRD patterns of LN, 0.1 %Co-LN, 0.5 %Co-LN, and 1 %Co-LN samples. c) The refinement result of 0.5 %Co-LN sample. d) The TEM images of 0.5 %Co-LN samples. e) The TEM and elemental mapping images of 0.5 %Co-LN samples.

indicating that the Co dopant promotes the lattice shrinkage. By comparing the ionic radii and valence state of Nb^{5+} ($r = 0.64$ Å@CN = 6) with those of Li^+ ($r = 0.76$ Å@CN = 6), Co^{3+} ($r = 0.55$ Å@CN = 6) and Co^{2+} ($r = 0.65$ Å@CN = 6) [34], it can be observed that Co^{3+}/Co^{2+} ions have a higher tendency to replace Nb^{5+} sites and lead to lattice shrinkage. From the high-resolution transition electron microscopy (HRTEM) images shown in Fig. 1d, the interplanar distance of the well-defined (0 1 2) plan for 0.5 %Co-LN is measured to be 3.56 nm. The morphology analysis shows that Co doping has little effect on the morphology of sample (Fig. 1d and S4). The EDS elemental mappings of all samples, as shown in Fig. 1e and S5, confirm that the elements Nb, O, and Co are homogeneously distributed in the examined region.

Raman detections were performed on the LN and 0.5 %Co-LN samples to investigate the fine structural information (Fig. 2a). The Raman spectrum of the LN and 0.5 %Co-LN show similar peaks compared to commercial $LiNbO_3$ powder [35]. The Raman shifts between 130–200 cm^{-1} (E-TO mode) correspond to the Nb-O vibrations [36], while the shifts between 345–490 cm^{-1} (E-TO mode) are associated with the bending modes of the Nb-O-Nb bond [35]. The A_1-TO peak observed around $\sim$ 592 cm^{-1} correspond to the symmetric stretching of Nb-O-Nb bond [37]. The FTIR spectra of LN and 0.5 %Co-LN are shown in Fig. S6. The broad peak around 714 cm^{-1} may correspond to the stretching

model of Nb-O octahedron [32,38,39]. XPS analysis was performed to investigate the chemical states of relevant elements in the pristine LN and 0.5 %Co-LN samples (Fig. 2b and S7–9). In Fig. 2b, the peaks at 530.4/530.3, 532.1/531.9, and 533.3/533.2 eV are attributed to lattice oxygen, V_O, and adsorbed oxygen on LN, respectively [40,41]. Importantly, the introduction of Co into LN significantly increased the content of V_O (Fig. 2b and S8), which may facilitate the light absorption of the material. The Nb 3d XPS spectra in LN and 0.5 %Co-LN exhibit two characteristic peaks (Fig. S9), located at 207.2/207.3 (Nb $3d_{3/2}$) and 209.9/210.0 eV (Nb $3d_{5/2}$) [42]. UV–visible diffuse reflectance spectra (DRS) of LN and 0.5 %Co-LN samples demonstrate that the introduction of Co broadens the absorption range and decreases the band gap from 3.59 eV to 3.49 eV (Fig. 2c and S10). Based on the XPS valence band spectra, the edge potentials of valence band maximum (VBM) for LN and 0.5 %Co-LN are measured to be $\sim$ 3.03 and $\sim$ 2.83 eV, respectively (Fig. S11). Combining the band gap and XPS valence band spectra, the conduction band edge potentials of LN and 0.5 %Co-LN are estimated to be $-$ 0.56 and $-$ 0.66 eV, respectively. The doping of Co ions can affect both conduction band (CB) and valence band (VB) energy levels of LN. Notably, the CB potential for Co-LN is higher than that of LN (Fig. 2d).

Extended X-ray absorption fine structure spectroscopy (EXAFS) of the Nb and Co K-edge of the sample together with the related reference
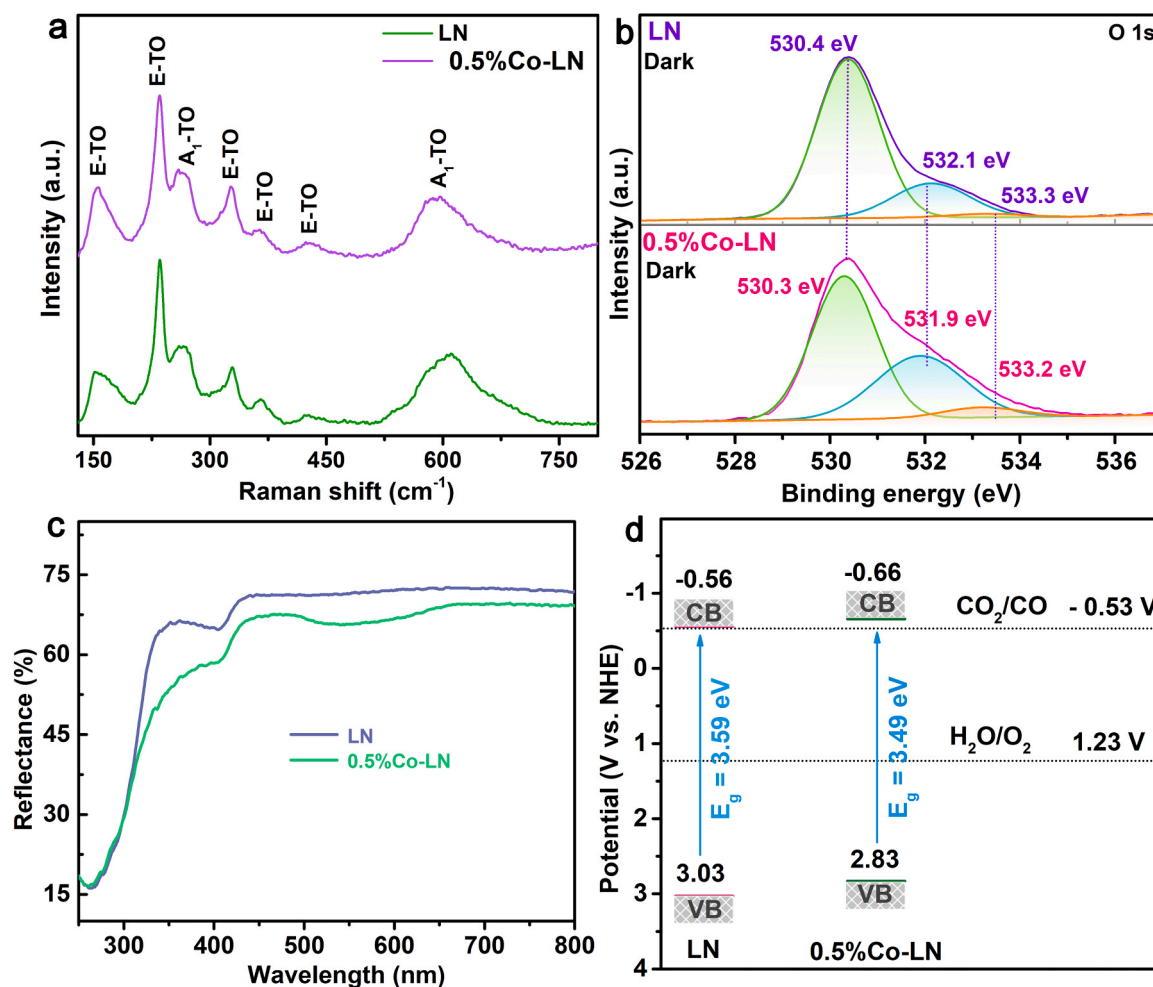
Fig. 2. a) The Raman spectra of the LN and 0.5 %Co-LN samples. b) High-ressolution XPS spectrum of O 1s spectra in LN and 0.5 %Co-LN samples under dark. c) The DRS for pure LN and 0.5 %Co-LN samples. d) The schematic of energy band alignments for LN and 0.5 %Co-LN.

materials were performed to probe the local coordination environment [43]. As shown in Fig. 3a, the Nb K-edge of LN and 0.5 %Co-LN is located between the Nb foil and Nb_2O_5, implying that the Nb has a positive charge between 0 and + 5 ($Nb^{\delta+}$, $0 < \delta < 5$) [44,45]. The Co K-edge of 0.5 %Co-LN is situated between the Co foil and Co_2O_3, closer to CoO, suggesting that the Co has a positive charge between 0 and + 3 ($Co^{\delta+}$, $0 < \delta < 3$) [7,44]. This is consistent with the result obtained from the Co 2p *in-situ* high-resolution XPS spectrum, which exhibits characteristic peaks for Co^{2+} and Co^{3+}. Quantitative least-squares EXAFS analysis was also conducted to further investigate the coordination configurations of Nb and Co in corresponding sample. The results are shown in Fig. 3c-d and S12, and the details are listed in Table S3 and S4. The Nb K-edge Fourier transform (FT)-EXAFS spectrum of LN and 0.5 %Co-LN shows prominent peaks at 1.899 Å and 1.907 Å (corresponding to Nb-O bonds) in the first shell, respectively [46,47]. Importantly, the coordination number decreases from 3.1 to 1.9, which is consistent with the XPS analysis result discussed in Fig. S8, indicating an increase in V_O content with the introduction of Co [48]. The Co FT-EXAFS spectrum of 0.5 % Co-LN exhibits a peak at 1.829 Å (Co-O) in the first shell [4], which is smaller than the Nb-O (1.899 Å) in LN. This implies that the Co ($Co^{2+/3+}$) with smaller ionic radii compared to Nb^{5+} would replace the Nb site and result in lattice shrinkage. Meanwhile, the Co FT-EXAFS spectrum of 0.5 %Co-LN at higher shells shows Co-Nb distances of 3.428 and 3.824 Å, which are smaller than the Nb-Nb distance (3.881 Å), further illustrating the replacement of Nb by Co. EXAFS wavelet transforms (WT) shown in Fig. 3e–g and S13 also highlight the shorter radial distance of Co-Nb introduction of Co.

The photocatalytic CO_2 reduction performance of the as-prepared materials was carried out at room temperature without the addition of co-catalysts or sacrificial agents. Control tests (Fig. S14a) confirm that both the photocatalyst and light irradiation are essential for the photo-catalytic CO_2 reduction in this testing system. In addition, when $^{13}CO_2$ and $H_2^{18}O$ are used as raw material for isotope detection (Figs. S14b-c), the results of mass spectrometry peaks clearly determine that the products contain ^{13}CO ($m/z = 29$) and $^{18}O_2$ ($m/z = 36$). The ^{18}O and ^{16}O in $^{18}O^{16}O$ is derived from the $H_2^{18}O$ and $H_2^{16}O$, respectively [49,50]. This indicates that the products CO are derived from CO_2 along with the generation of O_2. The Co-LN catalysts exhibit significantly improved photocatalytic activity towards CO_2 conversion to CO under irradiation compared to LN (Fig. 4a and S15). Among the Co-LN samples, the 0.5 % Co-LN sample demonstrates the highest CO production with a quantity of 284.2 μmol g^{-1} after 4 h of photo-irradiation, corresponding to a CO generation rate of 71.1 μmol g^{-1} h^{-1}, which is 3.8 times higher than that of pristine LN (18.9 μmol g^{-1} h^{-1}) and surpasses previously reported photocatalysts (Fig. 4b and Table S5). Importantly, the chromatographic analysis (Fig. S16) of the CO_2 photo-reduction by 0.5 %Co-LN indicates the exclusive formation of CO, demonstrating a 100 % product selec-tivity. The effect of light intensity on the product was also investigated. As can be seen in Fig. S17, the yields of CO of the 0.5 %Co-LN sample grow almost linearly with light intensity enhancement and irradiation time. Even under high light intensity irradiation, the sample can still maintain 100 % selectivity of CO. The apparent quantum yield (AQY) with 365 nm monochromatic irradiation for 0.5 %Co-LN are calculated to be about 0.62 %. The 0.5 %Co-LN catalyst shows a reduced
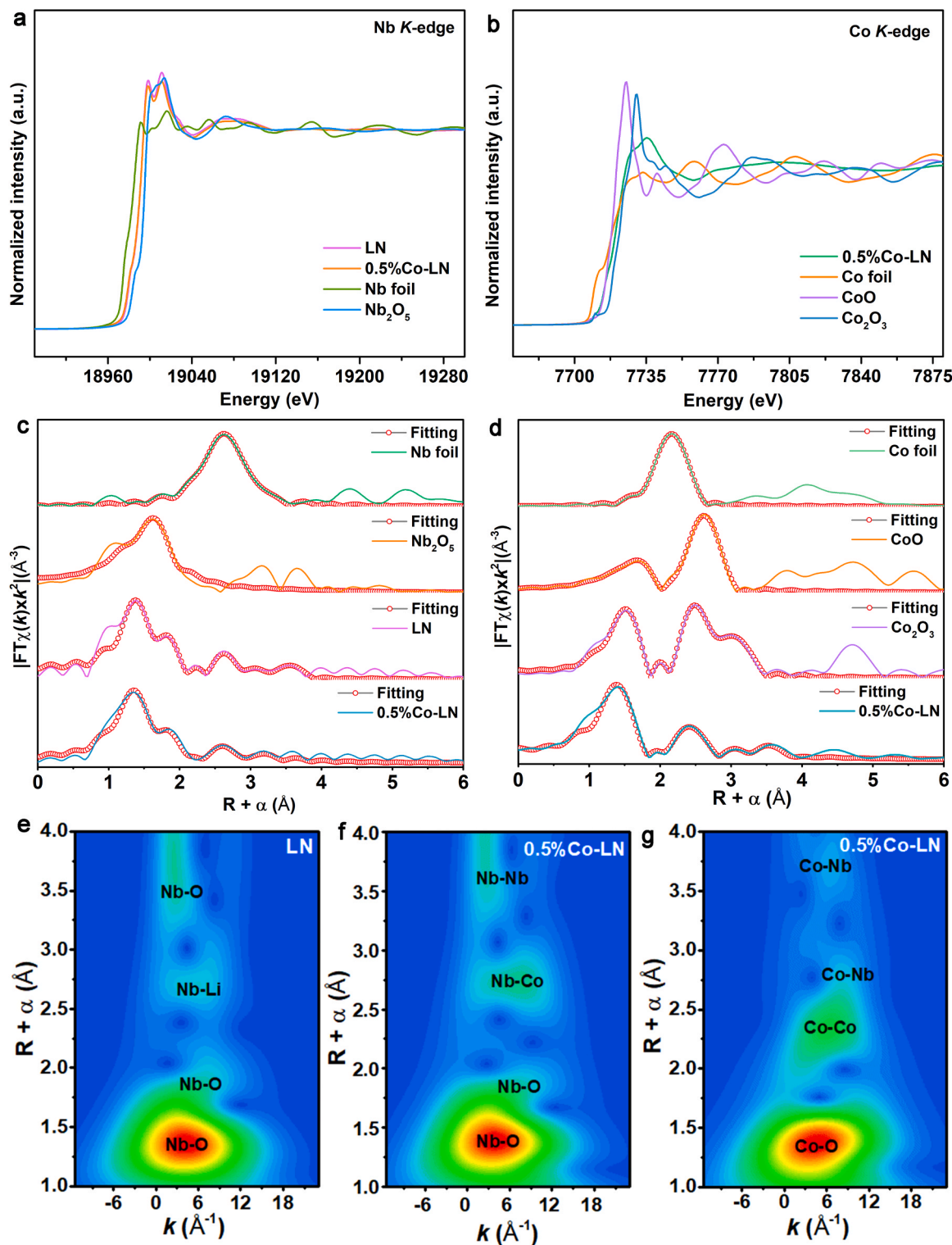
Fig. 3. a) Normalized Nb K-edge XAFS spectra for LN, 0.5 %Co-LN, Nb foil, Nb₂O₅. b) Normalized Co K-edge XAFS spectra for 0.5 %Co-LN, Co foil, CoO, and Co₂O₃. c) Nb and d) Co K-edge FT EXAFS spectra and the corresponding fitted curves for LN, 0.5 %Co-LN, Nb foil, Co foil, Nb₂O₅, CoO, and Co₂O₃ in R space. Wavelet transforms for the Nb K-edge EXAFS signals of e) LN and f) 0.5 %Co-LN. g) Wavelet transforms for the Co K-edge EXAFS signals of 0.5 %Co-LN.

electrochemical impedance spectroscopy (EIS) radius (Fig. 4c) and better photocurrent density (Fig. S18) compared to other samples, confirming that Co doping effectively improves the separation and transfer of photogenerated charge carriers [51,52].

The separation and transportation behaviors of photogenerated carriers were also investigated by the photoluminescence (PL) and time-resolved PL spectra to further understand the promotion effect of Co

dopant on the electron transfer dynamics [53,54]. The photoluminescence spectra of the LN and 0.5 %Co-LN samples are shown in Fig. S19a. Compared with the LN sample, the luminescence intensity of the 0.5 %Co-LN decreases, indicating that the electron-hole separation efficiency of Co-doping LN is improved. The average lifetimes (τ) turn out to be 2.77 and 2.81 ns for LN and 0.5 %Co-LN samples, respectively (Fig. S19b). The prolong lifetimes by Co doping indicate that the

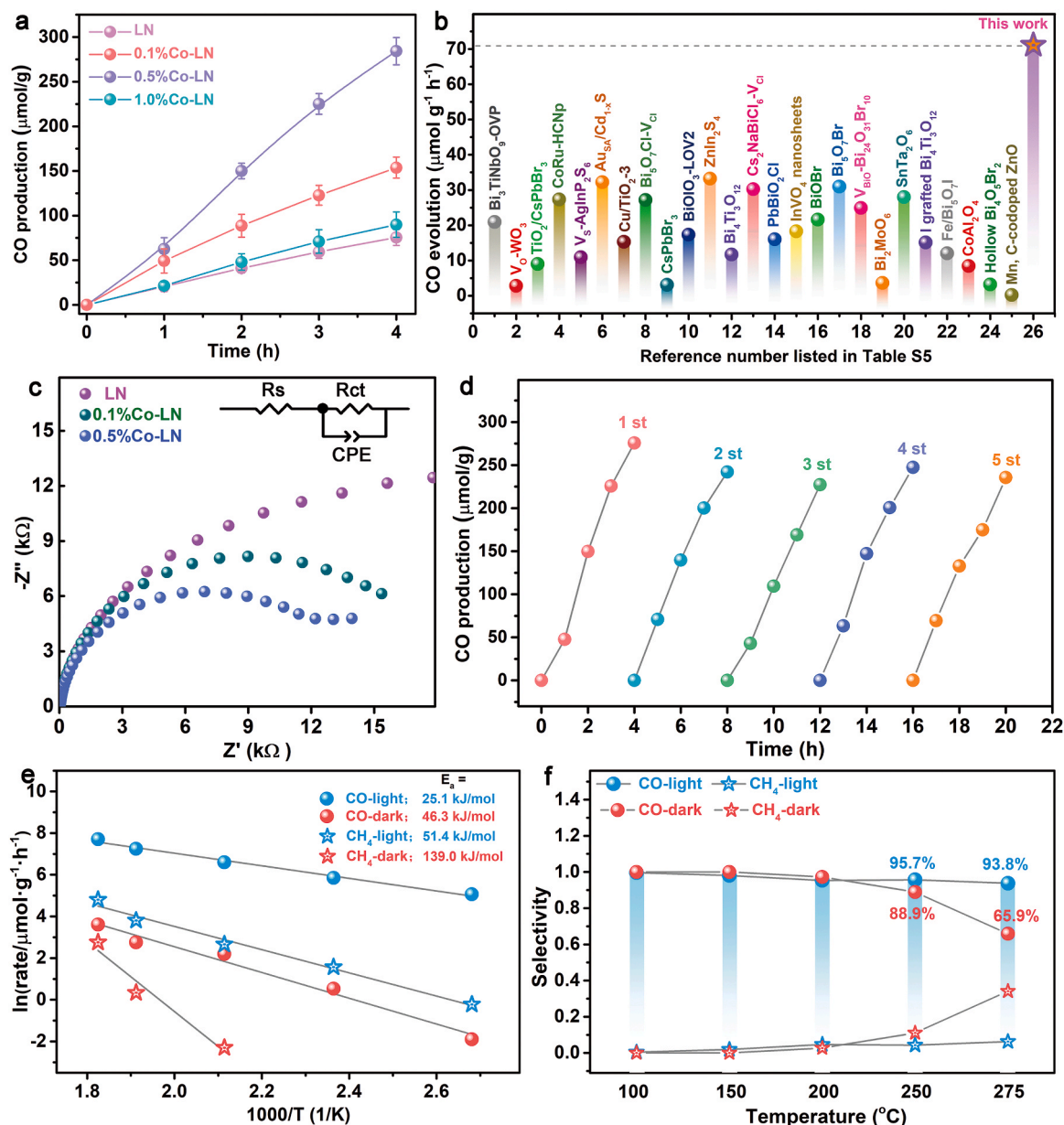**Fig. 4.** a) The time courses of photocatalytic CO evolution for LN and xCo-LN samples. b) Comparison with literature results of photocatalytic CO_2 reduction to CO. c) The EIS of the samples. d) Stability test of 0.5 %Co-LN sample after five cycles for 20 h. Arrhenius plots of e) CO and CH_4 formations under light and dark condition, obtained from the CO and CH_4 production rates at different temperatures using 0.5 %Co-LN sample. f) Comparison for the production selectivity of CO and CH_4 over 0.5 %Co-LN sample at different temperatures with and without light irradiation.

recombination between charges is mediated by trapping the electrons at Co sites [55].

Furthermore, a photocatalytic stability test was performed on the 0.5 %Co-LN composite (Fig. 4d), which showed no significant degradation in catalytic activity even after 20 h of the reduction reaction. Remarkably, the catalyst maintained its activity even after stored in air for eight months (Fig. S20), highlighting its excellent long-term stability. The structural stability of the 0.5 %Co-LN catalyst before and after photocatalysis was assessed by XRD, which showed no detection of other diffraction peaks after 12 h of irradiation compared to the fresh prepared 0.5 %Co-LN (Fig. S21), indicating its high optical stability.

The photothermal catalytic CO_2 reduction reaction was carried out on 0.5 %Co-LN at different temperature under light irradiation. Figs. S22-23 display the yield rates of CO and CH_4 for both photothermal catalysis and pure thermal catalysis. Under light irradiation, the CO production of 0.5 %Co-LN increases from 158.6 μmol g^{-1} h^{-1} to 2227.1

μmol g^{-1} h^{-1} as the temperature increases from 100 to 275 °C (Figs. S22f and S23e), which is higher than some reported materials listed in Table S6. Furthermore, CH_4 generation begins in the reduction products when the temperature exceeds 100 °C. Notably, the photothermal catalysis exhibits significantly higher production yield rates compared to pure thermal catalysis, with the CO yield in photothermal reactions being 18.3 times higher than that in pure thermal catalysis at 275 °C (Fig. S22f and S23e). This finding highlights the substantial enhancement of catalytic activity through light-induced hot carriers. The Arrhenius curves of ln(rate(CO)) and ln(rate(CH_4)) *vs* 1000/T were used to calculate the apparent activation energies (E_a) of CO and CH_4 in both photothermal catalysis and thermal catalysis, respectively. The calculated E_a values for CO and CH_4 in the photothermal catalysis are 25.1and 51.4 kJ mol^{-1}, respectively, which are significantly lower than the corresponding values of 46.3 and 139.0 kJ mol^{-1} in thermal catalysis (Fig. 4e). Moreover, as shown in Fig. 4f, the CO selectivity in

photothermal catalytic CO_2 reduction is much higher than that in the thermal catalysis. These findings indicate that light irradiation not only reduces the E_a of the CO_2 reduction reaction but also suppresses side reaction, resulting in enhanced catalytic activity and selectivity.

In-situ XPS measurements were employed to investigate electron transfer on the catalyst surface before, under, and after light irradiation, as shown in Fig. 5 and S24–25. Under light irradiation (purple line), the XPS spectra of O 1s and Nb 3d display a positive shift (Fig. 5a-b). The high-resolution XPS spectrum of the Co 2p component exhibit two spin-orbit split lines referred to as Co $2p_{3/2}$ and Co $2p_{1/2}$. The peaks at 781.1 ($2p_{3/2}$)/796.9 ($2p_{1/2}$) correspond to Co^{3+} oxidation states, while those at 781.1 eV ($2p_{3/2}$)/796.9 eV ($2p_{1/2}$) correspond to the Co^{2+} oxidation state [56,57]. Both Co $2p_{3/2}$ and Co $2p_{1/2}$ components exhibit corresponding satellite peaks at higher binding energy [57]. Under and after light irradiation for 1 h, the Co 2p binding energy shows a decrease trend (Fig. 5c and S25), which is opposite to that of Nb and O, indicating that some electrons of O and Nb return to Co with photo-excitation. ESR spectra were also performed to detect the presence of surface defects in

the catalyst, with and without light irradiation, as shown in Fig. 5d. The characteristic signal at g = 2.004 observed in both the LN and 0.5 % Co-LN samples indicates the presence of trapped electrons in V_O [40,46, 58]. Notably, the higher intensity of the ESR signal in 0.5 %Co-LN suggests a higher concentration of V_O compared to LN, demonstrating that Co doping enhances the concentration of V_O, consistent with the results from the O XPS survey (Fig. 2b). Furthermore, both the 0.5 % Co-LN and LN samples exhibit higher ESR signal intensity after light irradiation for 15 min, indicating the formation of V_O induced by light irradiation.

In-situ FTIR spectroscopy measurements were performed to investigate the photo-catalytic CO_2 conversion mechanism of Co-LN. To ensure that the adsorption of CO_2 and H_2O reaches equilibrium in the dark, the CO_2 adsorption process on 0.5 %Co-LN is recorded for 30 min (Fig. S26). The IR peaks correspond to H_2O, bidentate carbonates (b-CO_3^{2-}), HCO_3^-, and monodentate carbonates (m-CO_3^{2-}). The intensities of these peaks increase with longer adsorption time, indicating that CO_2 is adsorbed on the catalyst surface [59,60]. The CO_2 photo-reduction processes are
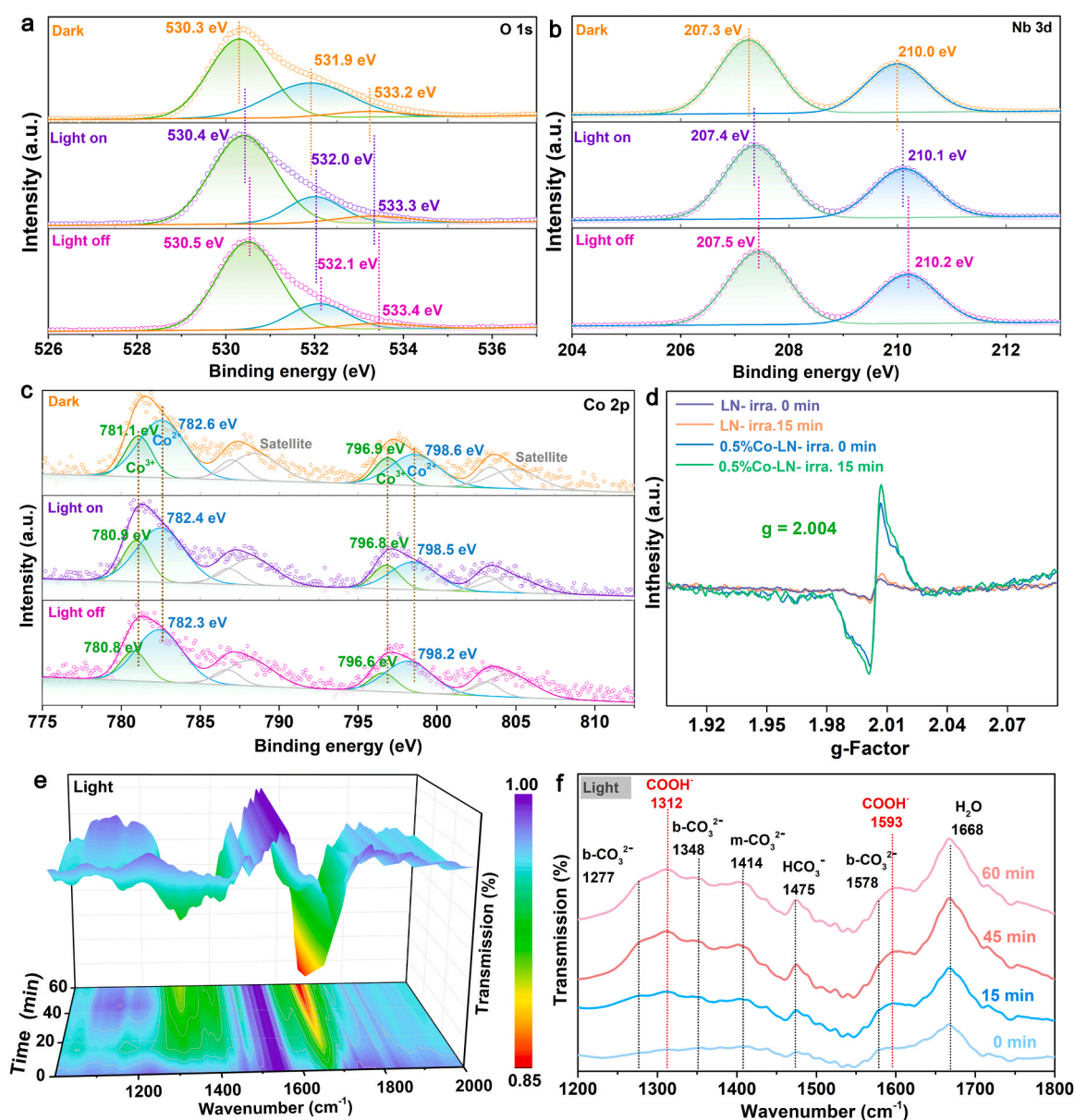

Fig. 5. In-situ XPS survey spectra of LN and 0.5 %Co-LN composites; O 1s a) and Nb 3d b) spectra of LN and 0.5 %Co-LN samples with light treatment; c) Co 2p spectra of 0.5 %Co-LN composite with light treatment. d) ESR spectra of LN and 0.5 %Co-LN with and without light irradiation. e-f) In-situ FTIR of CO_2 reduction reaction process of 0.5 %Co-LN at different time intervals, in which e) 3D color-map surface with projection.

shown in Fig. 5e–f. The peak at 1414 cm^{-1} is attributed to the asymmetric O-C-O stretch of monodentate (m-CO_3^{2-}), while a group of peaks appearing at 1277, 1348, and 1578 cm^{-1} correspond to the bidentate carbonate (b-CO_3^{2-}) [61–63]. The peak at 1475 cm^{-1} reveals the presence of CO_2 in the form of HCO_3^-. The peak at 1668 cm^{-1} is assigned to H_2O. Notably, the appearance of COOH$^-$ peaks at 1312 and 1593 cm^{-1}, which are typical intermediates in the CO_2-to-CO conversion [21,64–66], is observed. Furthermore, the intensity of these COOH$^-$ peaks exhibits an increasing trend with prolonged irradiation time.

Fig. 6a–c present the density of states (DOS) for LN, LN with V_O, and Co-LN with V_O samples. The conduction band (CB) minima in both samples are primarily dominated by Nb-4d states, while the valence band (VB) maxima are mainly attributed to O 2p states. Co doping results in a reduced band gap (2.95 eV of Co-LN with V_O vs. 3.54 eV of LN and 3.32 eV of LN with V_O), which is consistent with the result obtained from the DRS analysis. By comparing Fig. 6a with b, it can be found that the presence of V_O induces electron state distribution near the top of the CB, which is mainly contributed by Nb (Figs. S27-28). The higher content of V_O and Co doping create additional DOS between the CB and VB relative to the LN with V_O, thereby narrowing the bandgap and enhancing electron transport in photocatalytic CO_2 reduction process. Furthermore, the partial density of states for Co-LN with V_O shows that

the 3d orbitals of Co make a major contribution to the energy level between VB and CB (Figs. S29-30). This suggests that photogenerated electrons are more likely to migrate towards Co sites. The exposed (0 1 2) plan, identified through TEM analysis, is selected as adsorption surface for CO_2. The charge difference between LN with V_O and Co-LN with V_O demonstrates noticeable accumulation and consumption of charge near the V_O and Co sites, respectively (Fig. S31). The V_O and Co sites show the depletion of the charges, which facilitates the adsorption of the CO_2 molecules. After CO_2 adsorption, stronger charge interactions are observed between CO_2 and V_O in LN with V_O, as well as between CO_2 and Co-V_O couple in Co-LN with V_O, which favors the subsequent reduction processes. Quantitatively, the adsorption energy of CO_2 on LN and Co-LN with V_O increases by 0.64 eV and 0.61 eV, respectively, compared to LN (see Fig. 6d). The introduction of V_O and Co dopant enables CO_2 to form better coordinated adsorption configurations with more atoms, involving coordinated by nearby Nb atoms for LN with V_O, and coordinated by nearby Nb and Co atoms for Co-LN with V_O (Fig. S32). It is worth noting that the presence of V_O changes CO_2 adsorption from an endothermic process to an exothermic process (spontaneous), thereby facilitating the generation of subsequent intermediates. Combining the aforementioned calculation results with the findings from *in-situ* XPS and ESR measurements, it can be inferred that
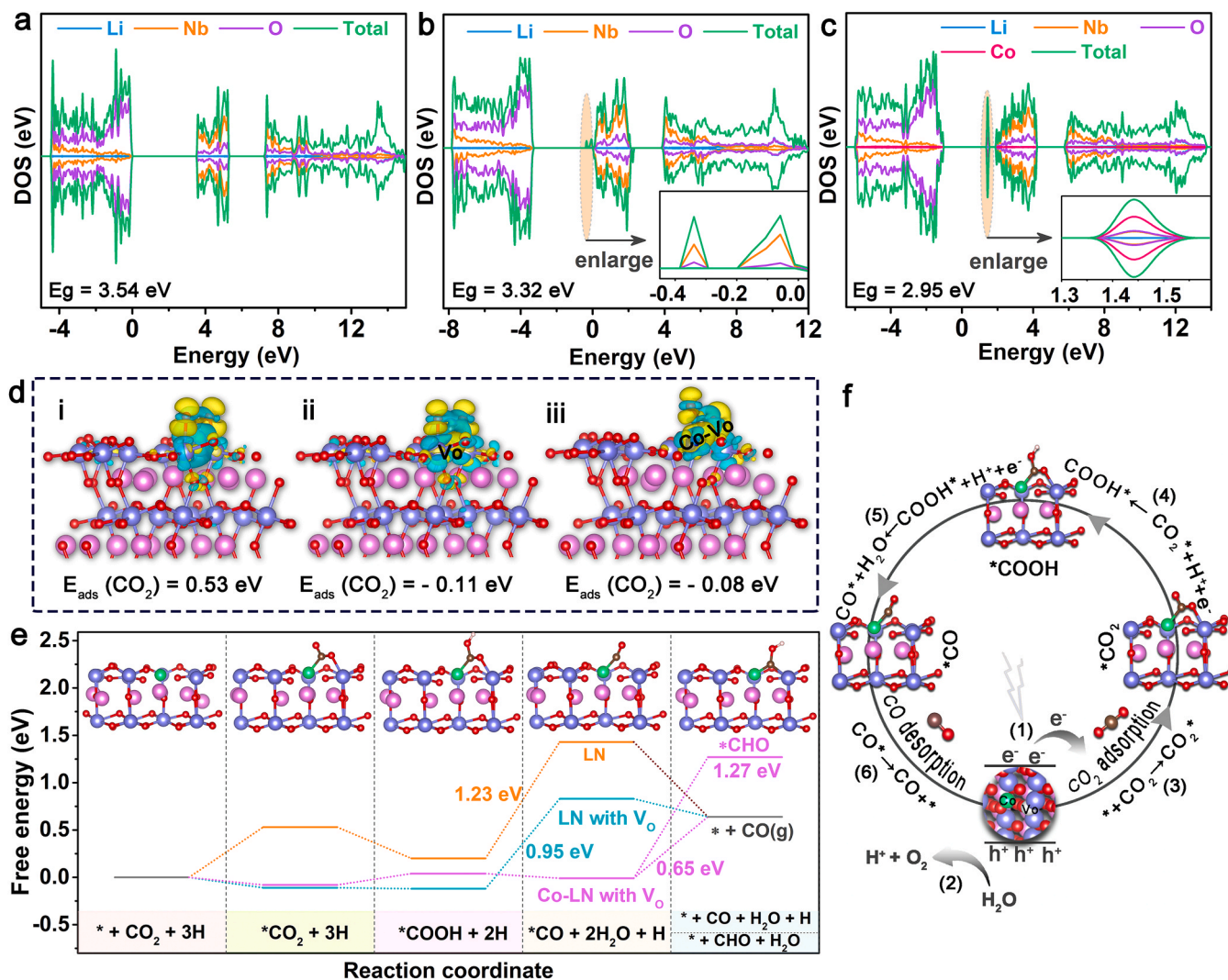

Fig. 6. The DOS of a) LN, b) LN with V_O, c) Co-LN with V_O. d) Schematic illustration of the adsorption of CO_2 molecules onto LN i), LN with V_O ii), and Co-LN with V_O iii) with the charge density difference. The yellow and cyan regions represent the charge accumulation and depletion, respectively. e) Free energy diagrams of CO_2 reduction to CO for prime LN, LN with V_O, and Co-LN with V_O structures. The inset shows the corresponding structure representation of the CO_2 reduction mechanism on Co-LN with V_O. f) The possible pathways of CO_2 photocatalytic reduction, where * indicates the adsorbed state.

under light irradiation, V_O and Co sites synergistically promote the adsorption and photocatalytic reduction of CO_2 to CO.

The influence of V_O and Co-doping in LN on the reaction Gibbs free energy (ΔG) is also investigated by DFT calculations, as shown in Fig. 6e. Examining the ΔG values reveals that the limiting step for primitive LN and LN with VO is the formation of the intermediate *CO, which is an endothermic process (+1.23 and +0.95 eV for LN and LN with V_O, respectively). While in Co-LN with V_O, the limiting step shifts to the desorption process of CO with a lower ΔG value of + 0.65 eV, indicating that the Co-doping has a profound effect on the charge distribution for the material. The introduced V_O dopant promotes the formation and stabilization of the intermediate $*CO_2$. Meanwhile, Co doping further enhances the stability of *CO intermediates. Furthermore, calculations for the formation of *CHO in Co-LN demonstrate that it is an endothermic process (ΔG: +1.27 eV). Therefore, it can be concluded that the photocatalytic reaction is more favorable to the CO desorption process, which contribute to its high selectivity for CO production.

Based on above analysis, we propose a feasible multi-electron series reduction mechanism to elucidate the pathway of CO_2 photoreduction, as illustrated in Fig. 6f and Table S7. When the sample is excited by light, electrons from the VB of Co-LN are excited to the CB, resulting in the generation of photoelectrons and holes (step 1). Subsequently, these electron-hole pairs migrate to the surface of catalyst, participating in the CO_2 photoreduction process. Compared to the oxidation potential of H_2O/O_2 at + 0.82 eV (*vs.* NHE), the VB potential of Co-LN is relatively positive at 2.83 eV (*vs.* NHE). This allows for the oxidation of H_2O to O_2, resulting in the generation of H^+ (step 2). CO_2 molecules adsorb onto the surface of the Co-LN photocatalyst, forming $*CO_2$ species (step 3). Following this, an electron reacts with $*CO_2$ and a H^+ ion to form COOH* species (step 4). The COOH* group is further reduced into a CO* and a H_2O molecule by a second photogenerated electron (step 5). Ultimately, after undergoing the characteristic two-electron process, the produced CO* molecules are dissociated from the catalyst's surface, yielding CO gas (step 6).

4. Conclusion

In conclusion, we find that the synergistic effect resulting from the dual-active-center formed in Co doping $LiNbO_3$ photocatalyst significantly reduce the activation energy of the rate-limiting step in the photoreduction of CO_2 to CO which leaded to the high activity and 100 % CO selectivity. Notably, the highest CO yield is up to 71.1 μmol g^{-1} h^{-1} for 0.5 %Co-LN, without the need for additional metal active species or sacrificial agents. Furthermore, it exhibits excellent durability, maintaining high activity even after several catalytic cycles and half year of catalyst preparation. The relevant characterizations reveal that the oxygen vacancy and Co-dopant stabilizes $*CO_2$ and *CO intermediates, respectively, regulating the rate-limiting step, ultimately facilitating high activity and 100 % selectivity in the photoreduction of CO_2 to CO. This study opens new possibilities for expanding the family of photocatalysts used in CO_2 reduction and facilitates the intensive investigation of the photocatalytic CO_2 reduction.

CRediT authorship contribution statement

Liangling Sun: Writing – original draft, Investigation, Formal analysis, Data curation. **Hairui Cai:** Resources, Investigation, Formal analysis. **Bin Wang:** Writing – review & editing, Supervision, Data curation. **Jingwen Xu :** Investigation, Formal analysis. **Xiaoxiao Zeng:** Methodology, Investigation, Formal analysis. **Chao Liang:** Writing – review & editing, Funding acquisition, Formal analysis. **Zhimao Yang:** Writing – review & editing, Supervision, Funding acquisition. **Shengchun Yang:** Writing – review & editing, Supervision, Investigation, Funding acquisition.

Declaration of Competing Interest

Data availability

No data was used for the research described in the article.

Acknowledgements

Appendix A. Supporting information

Supplementary data associated with this article can be found in the online version at doi:10.1016/j.apcatb.2024.123789.

References

[1] T. Hisatomi, K. Domen, Reaction systems for solar hydrogen production via water splitting with particulate semiconductor photocatalysts, Nat. Catal. 2 (2019) 387–399, https://doi.org/10.1038/s41929-019-0242-6.

[2] Y.Y. Birdja, E. Pérez-Gallent, M.C. Figueiredo, A.J. Göttle, F. Calle-Vallejo, M.T. M. Koper, Advances and challenges in understanding the electrocatalytic conversion of carbon dioxide to fuels, Nat. Energy 4 (2019) 732–745, https://doi.org/10.1038/s41560-019-0450-y.

[3] Z. Wang, Y. Inoue, T. Hisatomi, R. Ishikawa, Q. Wang, T. Takata, S. Chen, N. Shibata, Y. Ikuhara, K. Domen, Overall water splitting by Ta_3N_5 nanorod single crystals grown on the edges of $KTaO_3$ particles, Nat. Catal. 1 (2018) 756–763, https://doi.org/10.1038/s41929-018-0134-1.

[4] Y. Wang, G. Fan, S. Wang, Y. Li, Y. Guo, D. Luan, X. Gu, X.W.D. Lou, Implanting CoO_x clusters on ordered macroporous ZnO nanoreactors for efficient CO_2 photoreduction, Adv. Mater. 34 (2022) e2204865, https://doi.org/10.1002/adma.202204865.

[5] T. Ouyang, H.H. Huang, J.W. Wang, D.C. Zhong, T.B. Lu, A dinuclear cobalt cryptate as a homogeneous photocatalyst for highly selective and efficient visible-light driven CO_2 reduction to CO in CH_3CN/H_2O solution, Angew. Chem. Int. Ed. 56 (2017) 738–743, https://doi.org/10.1002/anie.201610607.

[6] S. Ji, Y. Qu, T. Wang, Y. Chen, G. Wang, X. Li, J. Dong, Q. Chen, W. Zhang, Z. Zhang, S. Liang, R. Yu, Y. Wang, D. Wang, Y. Li, Rare-earth single erbium atoms for enhanced photocatalytic CO_2 reduction, Angew. Chem. Int. Ed. 59 (2020) 10651–10657, https://doi.org/10.1002/anie.202003623.

[7] X. Xiong, C. Mao, Z. Yang, Q. Zhang, G.I.N. Waterhouse, L. Gu, T. Zhang, Photocatalytic CO_2 reduction to CO over Ni single atoms supported on defect-rich zirconia, Adv. Energy Mater. 10 (2020) 2002928, https://doi.org/10.1002/aenm.202002928.

[8] P. Hu, G. Liang, B. Zhu, W. Macyk, J. Yu, F. Xu, Highly selective photoconversion of CO_2 to CH_4 over $SnO_2/Cs_3Bi_2Br_9$ heterojunctions assisted by S-scheme charge separation, ACS Catal. 13 (2023) 12623–12633, https://doi.org/10.1021/acscatal.3c03095.

[9] J. Jiang, X. Wang, Q. Xu, Z. Mei, L. Duan, H. Guo, Understanding dual-vacancy heterojunction for boosting photocatalytic CO_2 reduction with highly selective conversion to CH_4, Appl. Catal. B 316 (2022) 121679, https://doi.org/10.1016/j.apcatb.2022.121679.

[10] L. Wang, P. Jin, S. Duan, H. She, J. Huang, Q. Wang, In-situ incorporation of Copper(II) porphyrin functionalized zirconium MOF and TiO_2 for efficient photocatalytic CO_2 reduction, Sci. Bull. 64 (2019) 926–933, https://doi.org/10.1016/j.scib.2019.05.012.

[11] Y. Wei, F. You, D. Zhao, J. Wan, L. Gu, D. Wang, Heterogeneous hollow multi-shelled structures with amorphous-crystalline outer-shells for sequential photoreduction of CO_2, Angew. Chem. Int. Ed. 61 (2022) e202212049, https://doi.org/10.1002/anie.202212049.

[12] Y. Wang, H. Huang, Z. Zhang, C. Wang, Y. Yang, Q. Li, D. Xu, Lead-free perovskite $Cs_2AgBiBr_6$@g-C_3N_4 Z-scheme system for improving CH_4 production in photocatalytic CO_2 reduction, Appl. Catal. B 282 (2021) 119570, https://doi.org/10.1016/j.apcatb.2020.119570.

[13] F. Raziq, K. Khan, S. Ali, S. Ali, H. Xu, I. Ali, A. Zada, P. Muhammad Ismail, A. Ali, H. Khan, X. Wu, Q. Kong, M. Zahoor, H. Xiao, X. Zu, S. Li, L. Qiao, Accelerating CO_2 reduction on novel double perovskite oxide with sulfur, carbon incorporation: Synergistic electronic and chemical engineering, Chem. Eng. J. 446 (2022) 137161, https://doi.org/10.1016/j.cej.2022.137161.

[14] L. Pan, H. Mei, G. Zhu, S. Li, X. Xie, S. Gong, H. Liu, Z. Jin, J. Gao, L. Cheng, L. Zhang, Bi selectively doped $SrTiO_{3-x}$ nanosheets enhance photocatalytic CO_2 reduction under visible light, J. Colloid Interface Sci. 611 (2022) 137–148, https://doi.org/10.1016/j.jcis.2021.12.033.

[15] X. Sun, Y. Xie, F. Wu, H. Chen, M. Lv, S. Ni, G. Liu, X. Xu, Photocatalytic hydrogen production over chromium doped layered perovskite Sr_2TiO_4, Inorg. Chem. 54 (2015) 7445–7453, https://doi.org/10.1021/acs.inorgchem.5b01043.

[16] K. Teramura, S.-i Okuoka, H. Tsuneoka, T. Shishido, T. Tanaka, Photocatalytic reduction of CO_2 using H_2 as reductant over $ATaO_3$ photocatalysts (A = Li, Na, K), Appl. Catal. B 96 (2010) 565–568, https://doi.org/10.1016/j.apcatb.2010.03.021.

[17] C. Xie, D. Yan, H. Li, S. Du, W. Chen, Y. Wang, Y. Zou, R. Chen, S. Wang, Defect chemistry in heterogeneous catalysis: recognition, understanding, and utilization, ACS Catal. 10 (2020) 11082–11098, https://doi.org/10.1021/acscatal.0c03034.

[18] J. Di, C. Chen, C. Zhu, R. Long, H. Chen, X. Cao, J. Xiong, Y. Weng, L. Song, S. Li, H. Li, Y. Xiong, Z. Liu, Surface local polarization induced by bismuth-oxygen vacancy pairs tuning non-covalent interaction for CO_2 photoreduction, Adv. Energy Mater. 11 (2021) 2102389, https://doi.org/10.1002/aenm.202102389.

[19] S. Vinoth, W.-J. Ong, A. Pandikumar, Defect engineering of BiOX (X = Cl, Br, I) based photocatalysts for energy and environmental applications: current progress and future perspectives, Coord. Chem. Rev. 464 (2022) 214541, https://doi.org/10.1016/j.ccr.2022.214541.

[20] Y. Ma, B. Qiu, J. Zhang, M. Xing, Vacancy engineering of ultrathin 2D materials for photocatalytic CO_2 reduction, ChemNanoMat 7 (2021) 368–379, https://doi.org/10.1002/cnma.202100051.

[21] H. Yu, J. Li, Y. Zhang, S. Yang, K. Han, F. Dong, T. Ma, H. Huang, Three-in-one oxygen vacancies: whole visible-spectrum absorption, efficient charge separation, and surface site activation for robust CO_2 photoreduction, Angew. Chem. Int. Ed. 58 (2019) 3880–3884, https://doi.org/10.1002/anie.201813967.

[22] G. Yang, J. Xiong, M. Lu, W. Wang, W. Li, Z. Wen, S. Li, W. Li, R. Chen, G. Cheng, Co-embedding oxygen vacancy and copper particles into titanium-based oxides (TiO_2, $BaTiO_3$ and $SrTiO_3$) nanoassembly for enhanced CO_2 photoreduction through surface/interface synergy, J. Colloid Interface Sci. 624 (2022) 348–361, https://doi.org/10.1016/j.jcis.2022.05.092.

[23] W. Chen, X. Liu, B. Han, S. Liang, H. Deng, Z. Lin, Boosted photoreduction of diluted CO_2 through oxygen vacancy engineering in NiO nanoplatelets, Nano Res. 14 (2020) 730–737, https://doi.org/10.1007/s12274-020-3105-1.

[24] Q. Zhang, P. Yang, H. Zhang, J. Zhao, H. Shi, Y. Huang, H. Yang, Oxygen vacancies in Co_3O_4 promote CO_2 photoreduction, Appl. Catal. B 300 (2022) 120729, https://doi.org/10.1016/j.apcatb.2021.120729.

[25] M. Wang, M. Shen, X. Jin, J. Tian, M. Li, Y. Zhou, L. Zhang, Y. Li, J. Shi, Oxygen vacancy generation and stabilization in CeO_{2-x} by Cu introduction with improved CO_2 photocatalytic reduction activity, ACS Catal. 9 (2019) 4573–4581, https://doi.org/10.1021/acscatal.8b03975.

[26] S. Wang, Y. Shan, W. Wang, D. Zheng, H. Liu, S. Liu, Y. Kong, J. Xu, Lone-pair electron effect induced a rapid photorefractive response in site-controlled $LiNbO_3$: Bi,M (M = Zn, In, Zr) crystals, Appl. Phys. Lett. 118 (2021) 191902, https://doi.org/10.1063/5.0048638.

[27] D. Tu, C.N. Xu, A. Yoshida, M. Fujihala, J. Hirotsu, X.G. Zheng, $LiNbO_3:Pr^{3+}$: a multipiezo material with simultaneous piezoelectricity and sensitive piezoluminescence, Adv. Mater. 29 (2017) 1606914, https://doi.org/10.1002/adma.201606914.

[28] I.C. Amaechi, A. Hadj Youssef, A. Dörfler, Y. González, R. Katoch, A. Ruediger, Catalytic applications of non-centrosymmetric oxide nanomaterials, Angew. Chem. Int. Ed. 61 (2022) e202207975, https://doi.org/10.1002/anie.202207975.

[29] L. Li, Y. Fan, Y. Li, X. Zhao, X. Cheng, Double-centers of V,Ce-Codoped $LiNbO_3$ from hybrid density functional theory calculations: electron trapping and excitation between the defect levels, Cryst. Growth Des. 20 (2020) 2774–2780, https://doi.org/10.1021/acs.cgd.0c00155.

[30] Y. Cui, Z. Wang, B. Li, Y. Yan, R. Xu, M. Meng, Y. Yan, Fluid-induced piezoelectric field enhancing photocatalytic hydrogen evolution reaction on g-C_3N_4/$LiNbO_3$/PVDF membrane, Nano Energy 99 (2022) 107429, https://doi.org/10.1016/j.nanoen.2022.107429.

[31] D. Mazkad, N.-e Lazar, A. Benzaouak, A. Moussadik, M. El Habib Hitar, N. Touach, M. El Mahi, E.M. Lotfi, Photocatalytic properties insight of Sm-doped $LiNbO_3$ in

[32] ferroelectric $Li_{1-x}NbSm_{1/3}xO_3$ system, J. Environ. Chem. Eng. 11 (2023) 109732, https://doi.org/10.1016/j.jece.2023.109732.

[32] X. Li, M. Zhang, J. Feng, C. Bai, Y. Ren, Electrostatic self-assembly to form unique $LiNbO_3$/ZnS core-shell structure for photocatalytic nitrate reduction enhancement, J. Colloid Interface Sci. 607 (2022) 1323–1332, https://doi.org/10.1016/j.jcis.2021.09.069.

[33] J. Wang, T. Bo, B. Shao, Y. Zhang, L. Jia, X. Tan, W. Zhou, T. Yu, Effect of S vacancy in Cu_3SnS_4 on high selectivity and activity of photocatalytic CO_2 reduction, Appl. Catal. B 297 (2021) 120498, https://doi.org/10.1016/j.apcatb.2021.120498.

[34] R.D. Shannon, Revised effective ionic radii and systematic studies of interatomic distances in halides and chalcogenides, Acta Cryst. A 32 (1976) 751–767, https://doi.org/10.1107/S0567739476001551.

[35] R.F. Ali, B.D. Gates, Synthesis of lithium niobate nanocrystals with size focusing through an ostwald ripening process, Chem. Mater. 30 (2018) 2028–2035, https://doi.org/10.1021/acs.chemmater.7b05282.

[36] M.K.R. Rahman, B. Riscob, R. Bhatt, I. Bhaumik, S. Ganesamoorthy, N. Vijayan, G. Bhagavannarayana, A.K. Karnal, L. Nair, Investigations on crystalline perfection, raman spectra and optical characteristics of transition metal (Ru) Co-doped Mg: $LiNbO_3$ single crystals, ACS Omega 6 (2021) 10807–10815, https://doi.org/10.1021/acsomega.1c00452.

[37] R.F. Ali, M. Bilton, B.D. Gates, One-pot synthesis of sub-10 nm $LiNbO_3$ nanocrystals exhibiting a tunable optical second harmonic response, Nanoscale Adv. 1 (2019) 2268–2275, https://doi.org/10.1039/c8na00171e.

[38] Z. Li, T. Yu, Z. Zou, J. Ye, Degradation in photocatalytic activity induced by hydrogenrelated defects in nano-$LiNbO_3$ material, Appl. Phys. Lett. 88 (2006) 071917, https://doi.org/10.1063/1.2175479.

[39] F. Yang, Q. Zhang, L. Zhang, M. Cao, Q. Liu, W.-L. Dai, Facile synthesis of highly efficient Pt/N-rGO/N-$NaNbO_3$ nanorods toward photocatalytic hydrogen production, Appl. Catal. B 257 (2019) 117901, https://doi.org/10.1016/j.apcatb.2019.117901.

[40] S. Yu, Y. Zhang, F. Dong, M. Li, T. Zhang, H. Huang, Readily achieving concentration-tunable oxygen vacancies in $Bi_2O_2CO_3$: triple-functional role for efficient visible-light photocatalytic redox performance, Appl. Catal. B 226 (2018) 441–450, https://doi.org/10.1016/j.apcatb.2017.12.074.

[41] J. Hao, Y. Zhang, L. Zhang, J. Shen, L. Meng, X. Wang, Restructuring surface frustrated Lewis acid-base pairs of BiOBr through isomorphous Sn doping for boosting photocatalytic CO_2 reduction, Chem. Eng. J. 464 (2023) 142536, https://doi.org/10.1016/j.cej.2023.142536.

[42] L. Sun, B. Wang, G. Xing, C. Liang, W. Ma, S. Yang, Bi-induced photochromism and photo-stimulated luminescence with fast photochromic response for multi-mode dynamic anti-counterfeiting and optical information storage, Chem. Eng. J. 455 (2023) 140752, https://doi.org/10.1016/j.cej.2022.140752.

[43] H. Funke, A.C. Scheinost, M. Chukalina, Wavelet analysis of extended x-ray absorption fine structure data, Phys. Rev. B 71 (2005) 094110, https://doi.org/10.1103/PhysRevB.71.094110.

[44] Y. Shen, C. Ren, L. Zheng, X. Xu, R. Long, W. Zhang, Y. Yang, Y. Zhang, Y. Yao, H. Chi, J. Wang, Q. Shen, Y. Xiong, Z. Zou, Y. Zhou, Room-temperature photosynthesis of propane from CO_2 with Cu single atoms on vacancy-rich TiO_2, Nat. Commun. 14 (2023) 1117, https://doi.org/10.1038/s41467-023-36778-5.

[45] X. Shi, Y. Huang, Y. Bo, D. Duan, Z. Wang, J. Cao, G. Zhu, W. Ho, L. Wang, T. Huang, Y. Xiong, Highly selective photocatalytic CO_2 methanation with water vapor on single-atom platinum-decorated defective carbon nitride, Angew. Chem. Int. Ed. 61 (2022) e202203063, https://doi.org/10.1002/anie.202203063.

[46] H. Yu, F. Chen, X. Li, H. Huang, Q. Zhang, S. Su, K. Wang, E. Mao, B. Mei, G. Mul, T. Ma, Y. Zhang, Synergy of ferroelectric polarization and oxygen vacancy to promote CO_2 photoreduction, Nat. Commun. 12 (2021) 4594, https://doi.org/10.1038/s41467-021-24882-3.

[47] J. Ha, J. Kim, R. O'Hayre, H. Lee, Substitutional behavior and dielectric property of $x(Na_{0.5}K_{0.5})NbO_3$-(1-x)$BaTiO_3$ using x-ray absorption fine structure spectroscopy, Ceram. Int. 41 (2015) 12027–12031, https://doi.org/10.1016/j.ceramint.2015.06.015.

[48] Y. Zhang, X. Zhi, J.R. Harmer, H. Xu, K. Davey, J. Ran, S.Z. Qiao, Facet-specific active surface regulation of Bi_xMO_y (M=Mo, V, W) nanosheets for boosted photocatalytic CO_2 reduction, Angew. Chem. Int. Ed. 61 (2022) e202212355, https://doi.org/10.1002/anie.202212355.

[49] X. Ren, M. Gao, Y. Zhang, Z. Zhang, X. Cao, B. Wang, X. Wang, Photocatalytic reduction of CO_2 on BiOX: effect of halogen element type and surface oxygen vacancy mediated mechanism, Appl. Catal. B 274 (2020) 119063, https://doi.org/10.1016/j.apcatb.2020.119063.

[50] Z.K. Xin, Y.J. Gao, Y. Gao, H.W. Song, J. Zhao, F. Fan, A.D. Xia, X.B. Li, C.H. Tung, L.Z. Wu, Rational design of dot-on-rod nano-heterostructure for photocatalytic CO_2 reduction: pivotal role of hole transfer and utilization, Adv. Mater. 34 (2021) 2106662, https://doi.org/10.1002/adma.202106662.

[51] L. Wang, H. Tan, L. Zhang, B. Cheng, J. Yu, In-situ growth of few-layer graphene on ZnO with intimate interfacial contact for enhanced photocatalytic CO_2 reduction activity, Chem. Eng. J. 411 (2021) 128501, https://doi.org/10.1016/j.cej.2021.128501.

[52] M. Yang, P. Wang, Y. Li, S. Tang, X. Lin, H. Zhang, Z. Zhu, F. Chen, Graphene aerogel-based NiAl-LDH/g-C_3N_4 with ultratight sheet-sheet heterojunction for excellent visible-light photocatalytic activity of CO_2 reduction, Appl. Catal. B 306 (2022) 121065, https://doi.org/10.1016/j.apcatb.2022.121065.

[53] Q. Zuo, R. Cui, R. Wang, Y. Wang, C. Yu, L. Wu, Y. Mai, Y. Zhou, High-loading single cobalt atoms on ultrathin MOF nanosheets for efficient photocatalytic CO_2 reduction, Sci. China Chem. 66 (2023) 570–577, https://doi.org/10.1007/s11426-022-1498-y.

[54] J. Park, J. Lim, J.Y. Lee, A silane-based host material with improved electron transport properties for phosphorescent OLEDs with high efficiency and low efficiency roll-off, Sci. China Mater. 66 (2023) 1997–2003, https://doi.org/10.1007/s40843-022-2342-x.

[55] K. Wang, M. Cheng, F. Xia, N. Cao, F. Zhang, W. Ni, X. Yue, K. Yan, Y. He, Y. Shi, W. Dai, P. Xie, Atomically dispersed electron traps in Cu doped BiOBr boosting CO_2 reduction to methanol by pure H_2O, Small 19 (2023) 2207581, https://doi.org/10.1002/smll.202207581.

[56] D. Montalvo, G. Corro, F. Bañuelos, O. Olivares-Xometl, P. Arellanes, U. Pal, Selective alcohols production through CO_2 photoreduction using Co_3O_4 /TiO_2 photocatalyst exploiting synergetic interactions between Ti^{3+}, Co^{2+} and Co^{3+}, Appl. Catal. B 330 (2023) 122652 https://doi.org/10.1016/j.apcatb.2023.122652.

[57] P. Gao, Y. Zeng, P. Tang, Z. Wang, J. Yang, A. Hu, J. Liu, Understanding the synergistic effects and structural evolution of $Co(OH)_2$ and Co_3O_4 toward boosting electrochemical charge storage, Adv. Funct. Mater. 32 (2021) 2108644, https://doi.org/10.1002/adfm.202108644.

[58] X. Chen, Y. Chen, X. Liu, Q. Wang, L. Li, L. Du, G. Tian, Boosted charge transfer and photocatalytic CO_2 reduction over sulfur-doped C_3N_4 porous nanosheets with embedded SnS_2-SnO_2 nanojunctions, Sci. China Mater. 65 (2021) 400–412, https://doi.org/10.1007/s40843-021-1744-5.

[59] X. Jiao, X. Li, X. Jin, Y. Sun, J. Xu, L. Liang, H. Ju, J. Zhu, Y. Pan, W. Yan, Y. Lin, Y. Xie, Partially oxidized SnS_2 atomic layers achieving efficient visible-light-driven CO_2 reduction, J. Am. Chem. Soc. 139 (2017) 18044–18051, https://doi.org/10.1021/jacs.7b10287.

[60] Z. Zhao, Z. Wang, J. Zhang, C. Shao, K. Dai, K. Fan, C. Liang, Interfacial chemical bond and oxygen vacancy-enhanced In_2O_3/CdSe-DETA S-scheme heterojunction for photocatalytic CO_2 conversion, Adv. Funct. Mater. 33 (2023) 2214470, https://doi.org/10.1002/adfm.202214470.

[61] X. Shi, X. Dong, Y. He, P. Yan, F. Dong, Light-induced halogen defects as dynamic active sites for CO_2 photoreduction to CO with 100 % selectivity, Sci. Bull. 67 (2022) 1137–1144, https://doi.org/10.1016/j.scib.2022.01.013.

[62] F. Chen, Z. Ma, L. Ye, T. Ma, T. Zhang, Y. Zhang, H. Huang, Macroscopic spontaneous polarization and surface oxygen vacancies collaboratively boosting CO_2 photoreduction on $BiOIO_3$ single crystals, Adv. Mater. 32 (2020) e1908350, https://doi.org/10.1002/adma.201908350.

[63] K. Yan, D. Wu, T. Wang, C. Chen, S. Liu, Y. Hu, C. Gao, H. Chen, B. Li, Highly selective ethylene production from solar-driven CO_2 reduction on the $Bi_2S_3@In_2S_3$ catalyst with In-SV-Bi active sites, ACS Catal. 13 (2023) 2302–2312, https://doi.org/10.1021/acscatal.2c05741.

[64] K. Niu, Y. Xu, H. Wang, R. Ye, H.L. Xin, F. Lin, C. Tian, Y. Lum, K.C. Bustillo, M. M. Doeff, M.T.M. Koper, J. Ager, R. Xu, H. Zheng, A spongy nickel-organic CO_2 reduction photocatalyst for nearly 100 % selective CO production, Sci. Adv. 3 (2017) e1700921, https://doi.org/10.1126/sciadv.1700921.

[65] Z. Guo, G. Chen, C. Cometto, B. Ma, H. Zhao, T. Groizard, L. Chen, H. Fan, W.-L. Man, S.-M. Yiu, K.-C. Lau, T.-C. Lau, M. Robert, Selectivity control of CO versus $HCOO^-$ production in the visible-light-driven catalytic reduction of CO_2 with two cooperative metal sites, Nat. Catal. 2 (2019) 801–808, https://doi.org/10.1038/s41929-019-0331-6.

[66] H. Zhang, Q. Liu, Z. Shen, Highly efficient photocatalytic conversion of CO_2 into CH_4 over Cu single atom promoted heterojunction: the effect of uplifted d-band center, Chin. Chem. Lett. 35 (2024) 108607, https://doi.org/10.1016/j.cclet.2023.108607.